

Why does the clustering of haloes depend on their formation history?

H.B. Sandvik^{1*}, O. Möller^{1*}, J. Lee² and S.D.M. White¹

¹ *Max Planck Institut für Astrophysik, D-85741 Garching, Germany*

² *School of Physics and Astronomy, FPRD, Seoul National University, Seoul 151-742, Korea*

8 June 2017

ABSTRACT

We discuss in the framework of the excursion set formalism a recent discovery from N-body simulations that the clustering of haloes of given mass depends on their formation history. We review why the standard implementation of this formalism is unable to explain such dependencies, and we show that this can, in principle, be rectified by implementing in full an ellipsoidal collapse model where collapse depends not only on the overdensity but also on the shape of the initial density field. We also present an alternative remedy for this deficiency, namely the inclusion of collapse barriers for pancakes and filaments, together with the assumption that formation history depends on when these barriers are crossed. We implement both these extensions in a generalised excursion set method, and run large Monte Carlo realisations to quantify the effects. Our results suggest that effects as large as those found in simulations can only arise in the excursion set formalism if the formation history of a halo does indeed depend on the size of its progenitor filaments and pancakes. We also present conditional distributions of progenitor pancakes and filaments for low-mass haloes identified at present epoch, and discuss a recent claim by Mo et.al. that most low-mass haloes were embedded in massive pancakes at $z \sim 2$.

Key words: methods: statistical – cosmology: theory – galaxies: clustering – galaxies: haloes – large-scale structure of Universe

1 INTRODUCTION

The excursion set formalism (Press & Schechter 1974; Bond et al. 1991; Bower 1991; Lacey & Cole 1993; Mo & White 1996) has been remarkably successful in describing several characteristics of the halo population in numerical simulations of structure formation, such as their unconditional and conditional mass functions, their merger rates, the halo bias and more. In general terms the approach implies picking a “particle” at random and smoothing the linear density field over ever smaller spheres around it, until the criterion for collapse at some redshift z is satisfied. The mass in the sphere is then identified as that of the collapsed object to which the particle belongs. This criterion is typically a constraint on the linear density contrast obtained from a collapse model, either spherical or ellipsoidal. The spherical collapse model gives a simple critical value for collapse $\delta_c \approx 1.686$ above which a patch is said to have collapsed at present time (Press & Schechter 1974). For the most popular implementations of the ellipsoidal

model this is modified only by making the collapse criterion scale-dependent $\delta_c(\sigma(R))$, because shape parameters are approximated by their expectation values (Sheth et al. 2001; Sheth & Tormen 2002). Thus determining whether a patch has collapsed or not requires knowledge only of the density contrast δ and the smoothing scale R .

When smoothing the density field a specific choice of filter shape must be used. An intuitively appealing choice is the top-hat filter for which both visualisation of the problem and the assignment of a mass to each collapsed region are straightforward. However, since the k -modes of the linear perturbation field are independent, it is mathematically more convenient to use a sharp k -space filter, since varying resolution then corresponds to a Markov random walk in the density contrast. As it turns out, this is also the filter which best reproduces the shape of mass functions seen in N-body simulations (Percival 2001), although a different filter then needs to be employed to assign a halo mass to each smoothing scale. It is surprising that this simple formalism, based only on the linear density field, is so successful in explaining many of the features seen in N-body simulations.

Despite its successes the approach clearly has shortcomings. Perhaps the most studied arises from the inapplicabil-

* E-mail: sandvik@mpa-garching.mpg.de (HBS); ole@mpa-garching.mpg.de (OM)

ity in detail of the physical model which underlies it. This stems from the fact that few particles actually lie at peaks of the smoothed initial density field. Most lie somewhere on the peripheral slopes of the peak associated with the halo they will actually belong to at the target redshift. As a result, there is a relatively poor match between the halo mass predicted for individual simulation particles by the random walk associated with the linear density field and the mass of the actual halos in which they find themselves as a result of the nonlinear evolution (Bond et al. 1991; White 1996; Sheth et al. 2001). The excellent agreement of the statistics of simulated halos with excursion set theory predictions thus does not extend to good object-by-object agreement. Bond & Myers (1996) devised an algorithm for explicitly taking account of the non-locality of the collapse process by assigning a surrounding “patch” to each “peak” in the initial conditions. This adds considerable complexity, however, and as a result is rarely used. Despite this problem, the excursion set approach has proved remarkably useful.

Another weakness which has received recent attention (Wang et al. 2006; Sheth & Tormen 2004, see also White 1996) is the fact that in its simplest and most used approximation, the approach does not allow correlations between halo properties defined by the character of the random walks on opposite sides of the barrier crossing. One example where such correlations are seen in simulations is the discovery by Gao et al. (2005) (GSW05) that old haloes are more clustered than young haloes of similar mass, or, more generally, that the clustering of halos depends on their formation history as well as on their mass (Croton et al. 2006, CGW06). This is also manifest as a dependence of clustering on properties such as halo concentration or substructure fraction (Wechsler et al. 2006). All these effects require some degree of correlation between environment density and halo formation history. In the standard 1-dimensional excursion set approach such correlations are impossible by construction.

There are two ways to extend the excursion set approach to address these effects. For a multidimensional random walk of the kind pioneered by Chiu & Lee (2001) (CL01) the extra variables can carry information across the barrier. A particle with a high environment density can cross at a different point in terms of these extra variables than a low density particle, and this can then be reflected in the random walk at smaller scales, hence in the formation history of the particle’s halo. A second way to account for such correlations arises if the “shape” of a halo’s formation history depends on *different* barriers than does its mass. For example, if we allow for the possibility that the assembly history of a halo could be significantly impacted by the size of its progenitor pancakes and filaments, an interesting scenario appears: it is then possible that the progenitor pancake scale is *larger* than the present halo scale, meaning the pancake barrier crossing lies between the halo collapse crossing and the scale defining the environment. This makes possible some correlation of formation history with environment density for halos of given mass, as seen in simulations. In this paper we will study both these possibilities in detail.

In order to allow for multi-scale correlations we implement the 6D Markov approach pioneered by CL01 using realisations of the deformation tensor rather than merely the density contrast, thereby utilizing the full shape information. We introduce a new set of shape parameters which al-

low us to construct a halo collapse barrier which reproduces very well the dynamical collapse model of Bond & Myers (1996) (BM96).

To be able to discuss the second possibility laid out above, we use the same dynamical collapse model to construct barriers corresponding to filaments and sheet formation. Such barriers were first presented in a recent paper by Shen et al. (2006), who used them, among other things, to provide interesting analytic estimates of the mass fractions in pancakes, filaments and haloes at any given time. Although they used the average shape approximation, something we will avoid here, their barriers could in principle also have been used for parts of the discussion in this paper. An alternative approach using the Zel’dovich approximation to discuss pancake formation was recently suggested by Lee (2006).

Our paper is laid out as follows. We first review the standard implementation of the excursion set method with flat and moving barriers and demonstrate why this is unable to reproduce the correlations discussed above. We then explain the generalisation of CL01 to a random walk in the deformation tensor. We show how choosing a particular linear combination of the eigenvalues allows the behaviour of the ellipsoidal collapse model to be successfully captured by barrier functions for haloes, filaments and sheets. We then run large samples of Monte Carlo realisations and analyse the results. We will conclude that it is possible to understand the clustering dependence on formation history if we make the plausible assumption that the latter depends on the masses of progenitor pancakes and filaments.

2 THE EXCURSION SET APPROACH

2.1 A random walk with a flat barrier

The spherical collapse model identifies a linear theory density contrast, $\delta_c(z) = \delta_c/D(z)$, extrapolated to present epoch, which corresponds to collapse at redshift z . Here $\delta_c \approx 1.686$ (Press & Schechter 1974) and $D(z)$ is the linear theory growth function normalised to 1 at $z = 0$. This equals $1/(1+z)$ in the special case of an Einstein de Sitter universe.

The traditional excursion set approach entails picking a random position (particle) and smoothing the linear density field, δ , over ever smaller spheres around this point until this spherical collapse criterion is fulfilled ($\delta \geq \delta_c(z)$).

The density perturbation smoothed over a scale R is given by

$$\delta_R(x) = \int \delta(x') W_R(x - x') d^3x', \quad (1)$$

where $W_R(x)$ is the scale-dependent smoothing filter. The variance of the density field on scale R is given by

$$\sigma^2(R) = \langle |\delta_R(x)|^2 \rangle = \frac{1}{4\pi^2} \int p(k) \tilde{W}_R^2(k) k^2 dk, \quad (2)$$

where $\tilde{W}_R(k)$ is the Fourier transform of the filter function. We are in principle free to choose this filter function, and the top-hat filter is frequently used for visualisation purposes, although computationally it is awkward since the added modes are correlated as we go to smaller scales. If instead a

hard k -space filter is used (with an upper k -space cutoff $k_c = 1/R$), the modes added by going to a smaller scale are statistically independent of the modes already included. Thus the density contrast performs a Markov random walk, and the entire problem can be described by such a random walk with an absorbing constant barrier, where σ^2 is the pseudo-time variable.

A particle trajectory will thus gradually carry out a random walk as σ^2 increases until the barrier is crossed at some particular value of this variance. This value corresponds to a smoothing scale R , and the mass of the corresponding halo is usually assigned using the top-hat formula (independent of the filter actually used for the smoothing);

$$M = \frac{4}{3}\pi\bar{\rho}R^3. \quad (3)$$

For the flat barrier, the problem of a Markov random walk with an absorbing barrier is analytically tractable. The first crossing distribution is given by (Chandrasekar 1943)

$$\nu f(\nu) = \left(\frac{\nu}{2\pi}\right)^{1/2} \exp\left(-\frac{\nu}{2}\right) \quad (4)$$

where $\nu = \delta_c^2/\sigma^2$.

The mass functions $n(m, z)$ of dark haloes are obtained from the density distribution function of up-crossings $f(\nu)$, through

$$\nu f(\nu) \equiv m^2 \frac{n(m, z)}{\rho} \frac{d \ln m}{d \ln \nu}. \quad (5)$$

It is important to realise that only the first crossing of a barrier is of any importance. Any subsequent crossings of the *same* barrier are irrelevant since collapse has already occurred at this redshift on a larger scale. However, an earlier redshift corresponds to a higher barrier, and the first up-crossing of this higher barrier corresponds to the largest scale on which collapse has occurred at the earlier redshift.

The conditional mass functions, defined as the distributions of progenitor mass at an earlier redshift for given final halo mass, are related to this two barrier problem. In the flat barrier case they are given by a simple extension of the unconditional mass function.

Although the excursion set approach cannot tell us about the substructure of a halo at any particular redshift, it does tell us something about how mass was *added* to the halo as it grew. This is possible since we can follow the mass of the halo's main progenitor with redshift, and thereby study its merger history (Lacey & Cole 1993). This allows us to identify the formation redshift z_f as the redshift at which we can first identify a progenitor with more than half the final mass.

2.2 The moving barrier

Sheth et al. (2001)(SMT01) were the first to use the ellipsoidal collapse model of BM96 in the excursion set approach. In this model collapse depends not just on the density field, but on eigenvalues of the tidal shear tensor. However, rather than drawing realisations of the shear tensor, and thereby including full shape information, SMT01 used expectation values of the shape parameters as a function of σ . They were then able to construct a collapse barrier whose value depended on the variance, σ^2 , thus on mass. Since variance

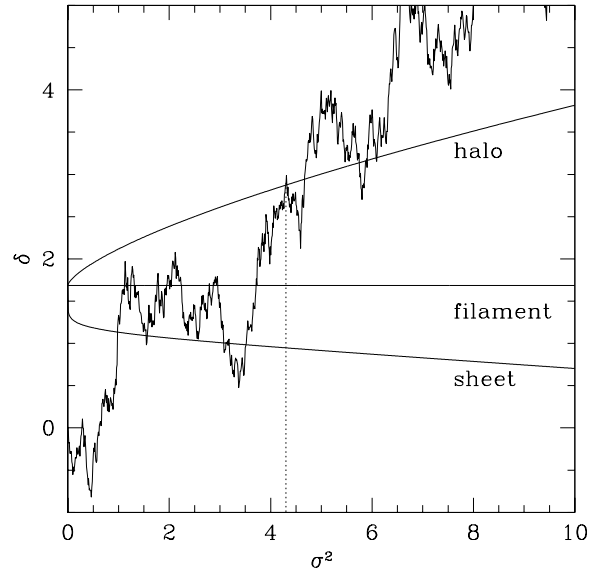


Figure 1. Example of a 1-dimensional random walk (jagged line) together with the average barriers for sheets, filaments and haloes at $z = 0$. The variance at which first up-crossing occurs determines the mass of each structure element in which this specific particle is embedded. It is clear that each halo identified at $z = 0$ is contained in a larger mass filament which is in turn contained in an even larger pancake. The environment density of the halo depends on values of δ on yet larger scales, nearer to $\sigma = 0$, whereas, in the usual formulation, its formation history is determined by the walk's structure on small scales to the right of halo crossing.

is the time-like variable, this has been labelled a “moving” barrier.

With this shortcut, the approach, with a sharp k -space filter, was highly successful in reproducing the shapes of the halo mass functions seen in N-body simulations. SMT01 provided a convenient analytic approximation to the first-crossing distribution corresponding to their moving barrier, but the symmetry which allows for compact representation of the conditional mass functions in the flat barrier case is lost.

As an extension to this work Shen et al. (2006) recently provided moving barriers which can represent collapse along one, two and three axes, corresponding to the formation of sheets, filaments and haloes, an effort which we replicate and extend later in this paper.

2.3 Correlations between clustering and formation

It is easy to see why the usual excursion set approach precludes correlations between large-scale environment and formation history for haloes of *given* mass (White 1996). Take the walk in figure 1 as an example. The walk crosses the $z = 0$ halo barrier at $\sigma_h^2 = 4.15$, and is so identified as belonging to a halo of mass $M(\sigma_h)$. The density of the large-scale environment for this particle can be identified using the values of δ near the origin, $\sigma^2 \ll \sigma_h^2$ (and $\delta \ll \delta_c$), whereas its formation history (at least, according to the usual definitions) depends on the behaviour of the random walk to the right of the barrier crossing at $\sigma_h^2 = 4.15$. Since, by

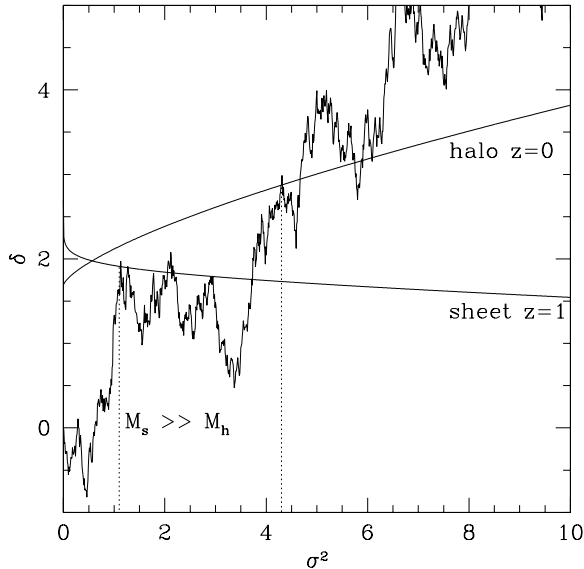


Figure 2. The random walk in figure (1) with the $z = 0$ halo barrier and $z = 1$ sheet barrier. This trajectory corresponds to a halo whose $z = 1$ progenitor was part of a pancake with mass exceeding the $z = 0$ halo mass. Assuming the assembly history of the final halo to be influenced by the mass of this early pancake provides a possible explanation for the dependence of clustering on formation history, since both the large-scale density and the mass of the early pancake correspond to points on the random walk to the left of the barrier crossing which defines the halo’s $z = 0$ mass.

assumption, all haloes of given mass cross the $z = 0$ halo collapse barrier at the same variance, the Markov nature of the random walk prevents any correlation between the two sides, between environment and formation history. In other words, old haloes should cluster in exactly the same fashion as young ones.

In the following we discuss two ways in which the excursion set approach can be extended to accommodate correlations between clustering and formation history. In the first, a multi-dimensional implementation of the random walk is combined with a non-spherical collapse barrier, as pioneered by Chiueh & Lee (2001). This implies that halo collapse at given mass is associated with a single constraint on a set of variables, in their case $\{\delta, r\}$. Formulated differently, the effective barrier for δ depends on the value of the shape parameter r . At barrier crossing δ and r can thus have different values for different halos (though they are perfectly correlated) and these different values can, in principle, correspond to different distributions of *both* formation history and large-scale environment. A correlation between environment and formation history thus becomes possible.

A second possibility is to stipulate that formation history of a halo somehow depends not only on its progenitor haloes, but on progenitor pancakes and filaments as well. These structures are characterized by collapse along one or two axes, respectively, and can be represented in the excursion set approach by different collapse barriers, as first suggested by Shen et al. (2006). Figure 1 compares the average shapes of such barriers at $z = 0$. The general trend is clearly very different as we go to smaller scales; the halo bar-

rier increases with σ^2 , the filament barrier is constant, and the pancake barrier actually decreases as we go to smaller scales. Since going to higher redshift simply scales the barriers up and to the right, it is possible, even probable for small masses, that the mass of a progenitor pancake at some early time is larger than the final mass of the halo. Figure 2 shows an example of such an occurrence, where the progenitor of a $z = 0$ halo was part of a larger mass pancake at $z = 1$. The idea that halo formation history could somehow depend on a different barrier than halo mass, is crucial, since there is every reason to expect a clear correlation between properties defined by the behaviour of the random walk on the same side of the barrier crossing which defines halo mass.

We have identified two independent extensions which can, in principle, accommodate the kind of correlation between environment and formation history that we seek. To examine whether these extensions can provide a quantitative explanation of the numerical results, we need to implement them in a generalised excursion set approach. This is the subject of the next section.

3 THE GENERALIZED EXCURSION SET METHOD

3.1 The 6D Random Walk

The general non-spherical excursion set approach with a hard k -space filter involves a random walk in the deformation tensor (the 2nd derivative tensor of the peculiar gravitational potential),

$$d_{ij} = \Phi_{,ij}, \quad (6)$$

rather than simply in the density contrast alone (which is the trace of this tensor). CL01 devised an algorithm for this:

The deformation tensor d can be simulated by drawing six independent Gaussian variables $\{y_1..y_6\}$ with dispersion σ_0 , and using the following linear transformation.

$$d_{11} = -\frac{1}{3} \left(y_1 + \frac{3}{\sqrt{15}} y_2 + \frac{1}{\sqrt{5}} y_3 \right) \quad (7)$$

$$d_{22} = -\frac{1}{3} \left(y_1 - \frac{2}{\sqrt{5}} y_3 \right) \quad (8)$$

$$d_{33} = -\frac{1}{3} \left(y_1 - \frac{3}{\sqrt{15}} y_2 + \frac{1}{\sqrt{5}} y_3 \right) \quad (9)$$

$$d_{12} = d_{21} = \frac{1}{\sqrt{15}} y_4 \quad (10)$$

$$d_{23} = d_{32} = \frac{1}{\sqrt{15}} y_5 \quad (11)$$

$$d_{13} = d_{31} = \frac{1}{\sqrt{15}} y_6. \quad (12)$$

This transformation satisfies the correlations of the deformation tensor as shown in Bardeen et al. (1986).

The random walk proceeds by drawing new values from the Gaussian distribution, and adding to y_i , until we have a walk of N steps. To each step n can be assigned a dispersion $\sigma^2 = n\sigma_0^2$.

For each step of the walk the deformation tensor can be diagonalised to find the three eigenvalues $\{\lambda_1, \lambda_2, \lambda_3\}$. This set of eigenvalues, along with a non-spherical collapse model, determine whether collapse has occurred by a given

redshift. Although the eigenvalues could be drawn directly from the probability distribution function of Doroshkevich (1970),

$$p(\lambda_1, \lambda_2, \lambda_3) = \frac{15^3}{2^3} \frac{1}{\sqrt{5}\pi\sigma_M^6} \exp\left(-\frac{3I_1^2}{\sigma_M^2} + \frac{15I_2}{2\sigma_M^2}\right) \quad (13)$$

$$\times (\lambda_1 - \lambda_2)(\lambda_2 - \lambda_3)(\lambda_1 - \lambda_3), \quad (14)$$

the above approach is significantly faster.

CL01 chose to avoid the diagonalisation process altogether by expressing the collapse criterion in terms of δ and of a variable r^2 directly calculable from the y_i s through two rotational invariants. This speeded up their calculations and allowed a nice visualisation of the problem. We discovered that this simplification results in a suboptimal representation of the fully 3-dimensional ellipsoidal collapse model, and we choose instead to use diagonalisation of the deformation tensor to obtain the the eigenvalues $\lambda_1, \lambda_2, \lambda_3$. The change of variables $\lambda_1, \lambda_2, \lambda_3 \rightarrow \delta, v, w$ given by

$$\delta = \lambda_1 + \lambda_2 + \lambda_3 \quad (15)$$

$$v = -\lambda_1 + \lambda_2 \quad (16)$$

$$w = -\lambda_1 - \lambda_2 + 2\lambda_3 \quad (17)$$

allows simple and accurate modelling of the behaviour of the ellipsoidal collapse model. This choice is discussed in detail in Appendix B.

3.2 Collapse Barriers

The spherical collapse barrier is found by applying the spherical collapse model and identifying the value of the initial density contrast, *linearly extrapolated* to present time, which corresponds to collapse at redshift z . It thus represents a constant (flat) barrier for the random walk. In the ellipsoidal collapse model, collapse is determined by the shape of the initial patch as well as its overdensity and this results in a barrier which depends on all 3 eigenvalues λ_i rather than just on their trace δ .

To fully capture this dependency we use the following barrier shape to represent halo collapse.

$$S_H(v, w, z) = \frac{\delta_c}{D(z)} [1 + \alpha_1 (vD(z))^{\alpha_2} + \alpha_3 (wD(z))^{\alpha_4}] \quad (18)$$

where $\delta_c = 1.686$ is the critical value for spherical collapse at the present epoch, $D(z)$ is the linear theory growth factor normalised to 1 at $z = 0$, and

$$\alpha_1 \approx 0.2809, \alpha_2 \approx 1.3557, \alpha_3 \approx 0.070, \alpha_4 \approx 1.41205 \quad (19)$$

The coefficients here were found by fitting to the collapse values of 8000 walks (stepsize $\Delta\sigma^2 = 0.025$) for which we used the full numerical solution to the ellipsoidal collapse model of BM96 (see appendix). This interpolation formula provides a near *perfect* fit to the true barrier obtained using the numerical solution, and it allows for a thorough investigation of the limitations and accuracy of the excursion set approach. We want to stress that our barrier was *not* found by fitting to N-body mass functions, but rather by requiring an accurate representation of the ellipsoidal collapse model of Bond & Myers (1996).

We also present barrier functions representing collapse along one and two axes. For sheets we have

$$S_S(v, w, z) = \frac{\delta_c}{D(z)} [1 - \alpha_1 (vD(z))^{\alpha_2} - \alpha_3 (wD(z))^{\alpha_4}] \quad (20)$$

where $\alpha_1 = 0.3748, \alpha_2 = 0.2399, \alpha_3 = 0.003237, \alpha_4 = 2.4187$. The formula for the filaments is slightly more complicated since it needs to reproduce halo-like behaviour for two large axes, and sheet-like behaviour for two short axes.

$$S_F(v, w, z) = \frac{\delta_c}{D(z)} [1 + \alpha_1 y D(z) (1 + \alpha_2 (x D(z))^{\alpha_3})] \quad (21)$$

where $\alpha_1 = 0.1104, \alpha_2 = 0.01641, \alpha_3 = 1.463$, and $x = w + 3v, y = w - 3v$. This change of variables is meaningful, since the condition of perfect triaxiality, for which the behaviour of the second axis is nearly identical to the spherical case (Shen et al. 2006), translates to $w = 3v$. Using the expectation values found in Appendix B, we can translate these barriers into “moving barriers” similar to Shen et al. (2006). These average barriers are the ones plotted in figure 1.

4 MONTE CARLO SIMULATIONS

To address the questions posed in section 2 we simulate a large ensemble ($\sim 10^6$) of random walks. For each simulated trajectory we output the density contrast on large scales along with the first up-crossings (actually the corresponding masses) of the halo, filament and sheet barriers (sec. 3.2) for a range of different redshifts. We also store the nominal formation redshift for the $z = 0$ halo, as well as the values of the auxiliary variables v and w at collapse. In the following we analyse the results and we try to understand their implications.

4.1 First crossing distributions

Figure (3) shows the simulated first crossing distributions for the halo barrier introduced in section 3.2 (squares) and for the spherical collapse barrier (triangles). These are compared with the corresponding analytic predictions from Press & Schechter (1974) and SMT01. It should come as no surprise that the distribution for our ellipsoidal collapse model is well fit by the SMT01 analytic formula, since this was obtained by fitting to a “moving barrier” version of our approach. Note that their final mass function contained an additional scaling parameter a , which allowed for better agreement with simulations. This degree of freedom is absent in our approach, though one might argue that it should, perhaps, be reintroduced when comparing our predictions to numerical results obtained with any particular (and to some extent arbitrary) definition of the boundary and thus the mass of a halo.

4.2 Correlations between large and small scales

As laid out in section 2.3 a multi-dimensional random walk with a shape-dependent barrier allows, in principle, for correlations between the environment density on large scale and the point at which the collapse barrier is crossed.

In the following we use our Monte Carlo sample of random walks to quantify this connection between large-scale overdensity, point of barrier crossing and, potentially, halo formation redshift.

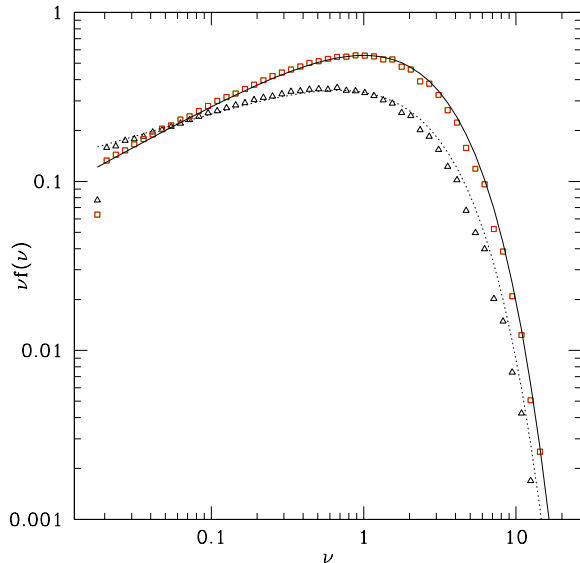


Figure 3. First crossing distributions obtained using the spherical collapse barrier (red squares) and the ellipsoidal collapse barrier presented in this paper (black triangles). The solid line is the analytical Press-Schechter solution, and the dotted line is the Sheth-Mo-Tormen approximation.

4.2.1 Environment density and point of barrier crossing

From our ensemble of walks we pick out those in the upper and lower 10% tails of the environment overdensity distribution (estimated as $\delta(\sigma^2 = 0.5)$). This represents, in a statistical sense, our most and least clustered haloes. We then compare the distributions of v/σ and w/σ at barrier crossing for the two sets. Concentrating on ratios removes the obvious dependence on σ , providing shape parameters which allow us to compare positions of barrier crossing in a way which does not depend on overall barrier scale.

For the ellipsoidal collapse barrier we find a clear albeit small correlation between environment and point of crossing. Both w and v are on average higher for walks with high environment density. The average value of v/σ is roughly 7 – 8% larger for the walks with high environment density than for walks in the low density tail. The dependence on w is somewhat less pronounced (5 – 6% difference between the two tails). As expected no such effects are found when we use the spherical collapse boundary.

It is worth noting that this effect is stronger for low values of σ^2 at barrier crossing (i.e. for massive haloes) than for less massive objects. This can be understood by recalling that the random walk is a diffusion process, so that correlations with values at “early times” (i.e. large scales, small variance values) are gradually washed out as “time/distance” increases (i.e. as variance increases). Throughout this work we define the environment by the overdensity at a fixed scale $\sigma^2 = 0.5$, roughly corresponding to $R \sim 10h^{-1}\text{Mpc}$ in the concordance ΛCDM cosmology we are adopting. With this definition it is not unexpected that environment correlates less with properties at barrier crossing as we go to smaller scales (larger σ^2 and smaller masses). This gives a first hint that the 6D excursion set approach will be unable to explain the effects measured by Gao et al.

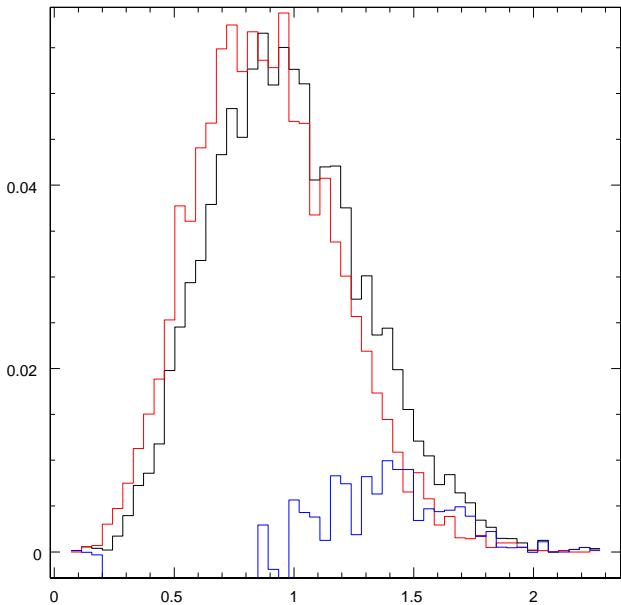


Figure 4. Histogram of e values at first crossing for the 10% highest (black) and 10% lowest (red) tails of environment density (estimated at $\sigma^2 = 0.5$) for the ellipsoidal collapse barrier. This plot refers to haloes more massive than the characteristic mass M_* . Although the effect is slight, the difference between the distributions is statistically highly significant. The values of e are on average $\sim 10\%$ larger at the point of first crossing for walks in the high environment density tail than for walks in the corresponding low density tail.

(2005), since these are largest for low mass haloes, and are virtually non-existent for the most massive haloes.

4.2.2 Clustering and Patch Shapes

It is perhaps more interesting to study environmental effects on collapse properties we are familiar with. For the purpose of this analysis we estimate the ellipticity and prolateness of the initial density field associated with a halo by

$$e = (-\lambda_1 + \lambda_3)/\sigma \quad (22)$$

and

$$p = (\lambda_1 - 2\lambda_2 + \lambda_3)/\sigma \quad (23)$$

We find that there is a weak correlation between environment density and the pre-collapse ellipticity of haloes (see eqn.(22) for the relevant definitions). Again we see that the effect fades as we go to smaller masses. Figure (4) shows histograms of e values for the 10% tails of the distribution in environment density for haloes with $M > M_*$. A corresponding plot for haloes with $M < 10^{-2}M_*$ shows no discernible difference between the two distributions. Roughly speaking, for massive haloes, those with the 10% highest (lowest) environment densities have ellipticities which are systematically 5% higher (lower) than those of typical haloes. Systematic effects with prolateness are also clear, albeit smaller, indicating that haloes in dense environments have a wider than

typical range of prolateness values - in agreement with the results for the ellipticities.

These results show that haloes in dense regions originate from more elliptical initial patches than less clustered objects of similar mass. It is tempting to extrapolate this conclusion to apply to the actual ellipticity of the collapsed, quasi-equilibrium halo. This is speculative, however, since we do not know how (or even if) the final shape of a halo is related to the shape of its initial patch.

4.2.3 Environment Density and Formation Redshift

In sections (4.2.1 and 4.2.2) we established that there is a small but clear correlation between environment overdensity and the point of barrier crossing, thus with the shape of the collapsing patch. The point of barrier crossing clearly influences the properties of the random walk at larger variance, hence on smaller mass scales, so we may expect a correlation between environment density and formation redshift. This is precisely what was detected in N-body simulations by Gao et al. (2005). They show that low-mass haloes with high formation redshifts are significantly more clustered than similar mass but late-forming objects. Hence they sit in denser environments.

We want to compare our results as directly as possible with the results of GSW05. They look at a sample of haloes with particle numbers in the range 100-200. Each particle has a mass of $8.6 \times 10^8 h^{-1} M_\odot$, so this corresponds roughly to $\sim 1 - 2 \times 10^{11} h^{-1} M_\odot$. In terms of the characteristic mass $M_* = 6.15 \times 10^{12} M_\odot$ this is roughly $M = 0.14 - 0.28 \times M_*$.

We try to replicate this by taking similar samples from our random walks. We use an effective power spectrum index of $n = -2$, and look at two mass bins, with masses in the ranges $M = [M_*, 2M_*]$, and $M = [0.02M_*, 0.1M_*]$. To improve statistics we use larger bins than GSW05 and we compare environment overdensity for haloes in the 20% (rather than 10%) tails of the distribution of formation redshift.

Despite these attempts at improving our statistical leverage, we are unable to find any effect whatsoever. We strongly exclude anything of the magnitude seen by GSW05. Our results therefore appear to rule out this idea as a potential model for the effects seen in the simulations.

This should not take us entirely by surprise, since the results of the previous section lead us to expect that any effect should be larger for the high-mass than for low-mass haloes. This is opposite to the numerical result. We conclude that although a formal dependence should be present, it is far too small to measure and cannot explain the results of GSW05 and CGW06.

4.3 Clustering and progenitor pancakes and filaments

Since our multi-dimensional extension of the excursion set approach is unable to reproduce the required correlation between clustering and formation history, we now turn to the other possibility laid out in section 2.3, namely that the correlation may reflect a dependence of formation history on the properties of progenitor pancakes and filaments. In particular we study the correlation between the masses of

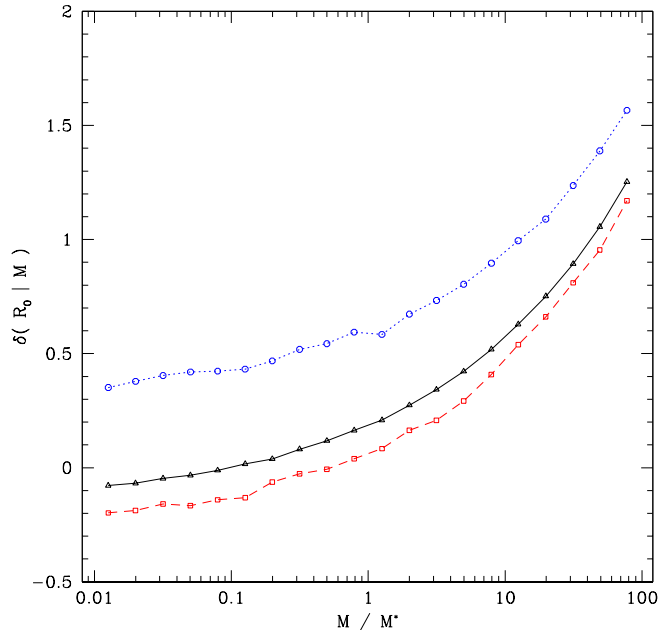


Figure 5. Average density at large scale ($R_0 \sim 10h^{-1}\text{Mpc}$) around a $z = 0$ halo, as a function of halo mass (black curve) together with the same quantity for halo subsets defined so that the progenitor pancakes at $z = 2$ lie in the upper (blue curve) and lower (red curve) 10% tails of the pancake mass distribution.

these progenitor structures and the large-scale environment of the $z = 0$ halo.

Figure 5 plots average large-scale ($\sim 10h^{-1}\text{Mpc}$) environment overdensity as a function of halo mass, and compares this with the values found using only those haloes whose progenitor pancakes at $z = 2$ lie in the upper or in the lower 10% tail of the pancake mass distribution. There is a strong correlation between this large-scale overdensity and the mass of the progenitor pancake, with haloes in denser environments tending to have more massive progenitor pancakes. The strength of this effect is greatest for low-mass haloes.

Fig. 6 shows a similar plot of large-scale environment overdensity as a function of halo mass, but now sorting haloes by progenitor filament mass at $z = 2$. A dependence is again clear, but is much weaker than was the case for progenitor pancakes. The smallness of the effect in this case is due to the fact that very few haloes were embedded in higher mass filaments at $z = 2$. Only for these haloes is any correlation between environment and progenitor filament mass to be expected, as explained in sec. (2.3).

We have established a clear correlation between environment overdensity at large scales and the mass of progenitor pancakes and filaments. If the formation history of a halo is somehow affected by the size of its progenitor pancakes and filaments, this correlation will induce a correlation between clustering and formation history. Intriguingly the effect is largest for low-mass haloes and becomes quite weak for the most massive haloes. This is precisely the behaviour found by GSW05 and CGW06, where the measured effects are only strong for haloes less massive than $\sim 10^{13} M_\odot$. In

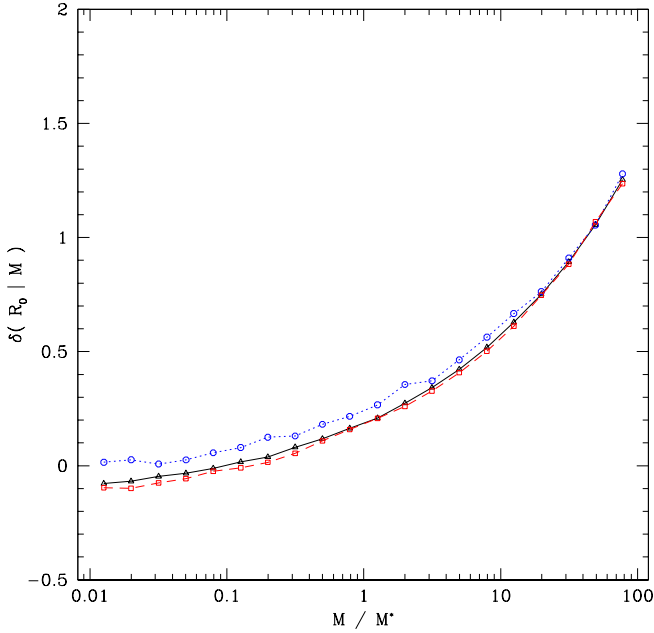


Figure 6. Average density at large scale ($R_0 \sim 10h^{-1}\text{Mpc}$) around a $z = 0$ halo, as a function of halo mass (black curve) together with the same quantity for halo subsets defined so that the progenitor filaments at $z = 2$ lie in the upper (blue curve) and lower (red curve) 10% tails of the filament mass distribution.

the schematic treatment of this section, the mass at which the dependence becomes small is dependent on whether we consider filaments or pancakes, and on the redshift at which we consider them to be relevant.

It is beyond the scope of the current discussion to present a detailed model for the dependence of halo formation history on the properties of progenitor pancakes and filaments. Such a connection is intuitively appealing, however, and we expect this to be an area where further analytic modelling will be very fruitful.

4.4 Pre-heating by pre-virialization?

Our barriers for collapse along one or two axes also allow us to address a recent claim by Mo et al. (2005) that the material which now resides in low-mass haloes ($M \lesssim 10^{12}M_\odot$) was pre-heated by the collapse of larger-scale pancakes (typical mass $M \sim 5 \times 10^{12}M_\odot h^{-1}$) at $z \sim 2$, and that as a result the gas component of many of these haloes failed to cool and form stars. The analytic argument underlying this claim was based on a simplified calculation which specifically failed to include the conditional distribution of the masses of progenitor pancakes for haloes of given $z = 0$ mass. We are now well equipped to carry out a more precise calculation of the relevant quantities.

To examine this claim we pick out haloes in narrow mass ranges around $M = 10^{12}M_\odot$, $M = 10^{11}M_\odot$ and $M = 10^{10}M_\odot$, and we look at the mass distribution of their progenitor pancakes and filaments at redshifts 1, 2, and 3. These cumulative distributions are shown in figs. (7) (pancakes) and (8) (filaments). They show that many low-mass

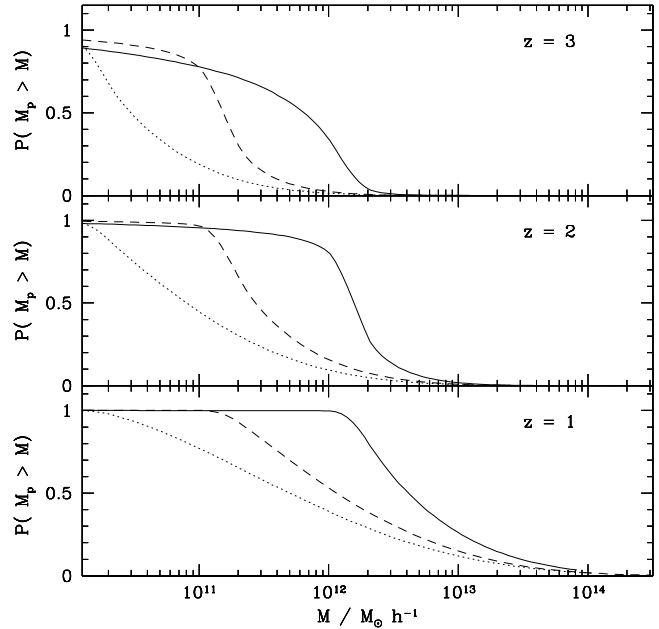


Figure 7. Cumulative distribution of progenitor pancake masses at several redshifts for haloes of $z = 0$ mass $10^{12}M_\odot$ (solid), $10^{11}M_\odot$ (dashed) and $10^{10}M_\odot$ (dotted). At $z = 2$ only $\sim 10\%$ of $10^{12}M_\odot$ haloes had progenitor pancakes of the size suggested by Mo et al. (2005). For $10^{11}M_\odot$ and $10^{10}M_\odot$ haloes this fraction is significantly smaller. Note that almost all haloes in these mass ranges were embedded in larger mass pancakes at $z = 1$. At $z = 3$ this fraction is 30% for the $10^{12}M_\odot$ haloes but is still large ($\sim 80\%$) for the smaller mass ranges.

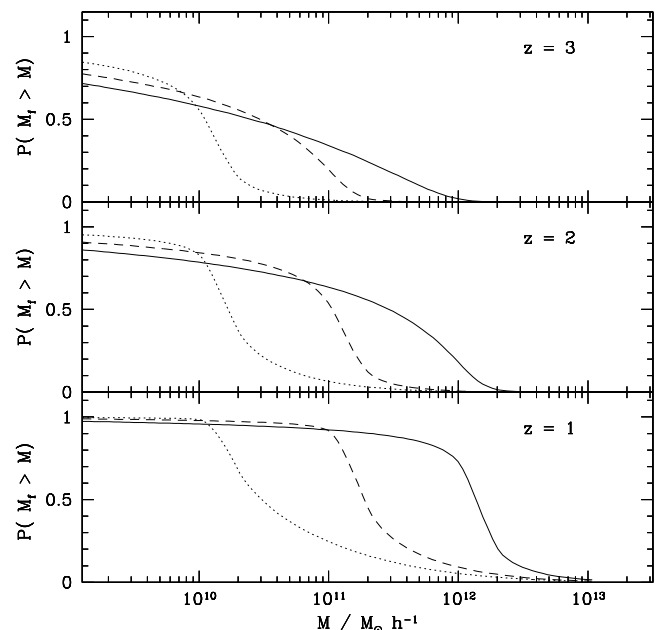


Figure 8. Cumulative distribution of progenitor filament masses at several redshifts for haloes of $z = 0$ mass $10^{12}M_\odot$ (solid), $10^{11}M_\odot$ (dashed) and $10^{10}M_\odot$ (dotted).

haloes were indeed embedded in larger mass structures at redshifts $z \sim 1 - 2$, in qualitative agreement with Mo et al. (2005).

Quantitatively however, the mechanism looks less promising. Central to the argument of Mo et al. (2005) was the assumption that most low-mass haloes were embedded in pancakes of mass $M \sim 5 \times 10^{12} M_\odot$ at $z \sim 2$. This was required to ensure sufficient preheating of gas to affect later condensation and star formation. From the middle graph in fig. (7) it is clear that typical $10^{11} M_\odot$ haloes had progenitor pancakes of mass $M \sim 2 \times 10^{11} M_\odot$ at $z = 2$, and only a few percent have progenitor pancakes as massive as assumed by Mo et al. (2005). The situation is even worse for typical $10^{10} M_\odot$ haloes which were embedded in pancakes of mass $M \sim 7 \times 10^{10} M_\odot$ at $z = 2$, nearly two orders of magnitude less than the required value.

Our results contradict those of Mo et al. (2005) in two ways. According to our analysis, progenitor pancake mass is not independent of halo mass in the way they suggest, and even for relatively massive “dwarf galaxy” haloes, the progenitor pancakes are typically too small to generate the temperatures required for suppression of later cooling. Taking both these discrepancies into account, it seems unlikely that the Mo et al. (2005) mechanism can account for the shallow faint end slope of the galaxy luminosity function and the relatively small number of luminous satellites around galaxies like the Milky Way.

5 CONCLUSIONS

We have used the excursion set formalism to discuss the correlation between environment and formation history found for haloes in large-scale simulations of cosmic structure formation. We implemented a multi-dimensional generalisation of the excursion set approach which assumes halo formation to follow the triaxial collapse model of Bond & Myers (1996) and which does not require further simplifying assumptions of the kind introduced by Sheth et al. (2001) to reduce the system to a 1-dimensional barrier crossing problem. A correlation between halo formation history and halo environment is expected in this model (Wang et al. 2006) but we have shown here that it is very weak. We *did*, however, demonstrate that there is a measurable correlation between environment density and the pre-collapse shape of a halo.

It appears that haloes in dense regions have slightly more extreme axial ratios than similar mass objects in underdense environments. This could potentially be studied with N-body simulations, although we caution that our definition of ellipticity, eqn.(22), while mathematically convenient, is not simply related to the measurable shape of non-linear, quasi-equilibrium haloes. To address this issue properly, we suggest using large N-body simulations such as the Millennium Simulation (Springel et al. 2005). It would be feasible to follow particles which are part of $z = 0$ haloes back to the initial density field. With a large enough sample of haloes one could then determine how the final shapes of halos are related to the properties of their initial, linear “patches”.

With straightforward definitions of environment density and halo formation time our multi-dimensional random

walks are inconsistent with the environment-formation history correlations found by GSW05 and CGW06. We have, however, discovered a different mechanism which can induce a dependence of some aspects of halo formation on halo environment. Crucial to our analysis of this mechanism are the collapse barriers for haloes, filaments and sheets introduced in section (3.2). We showed that many low-mass $z = 0$ haloes were embedded in larger-mass progenitor pancakes at redshifts $z \sim 1 - 2$, and that the mass of these progenitors correlates with the density of the environment surrounding the $z = 0$ haloes. Thus, if the formation history of $z = 0$ haloes is affected by the mass of their high-redshift progenitor pancakes, we can expect an induced dependence of formation history on environment. Although we do not attempt to model this, we show that sorting haloes by the mass of their progenitor pancakes at $z \sim 1$ to 3 gives a variation of mean environment with pancake mass which is of similar size and has a similar dependence on halo mass to the variation found in simulations when haloes are ranked by their formation time. Future efforts should result in a more detailed model for the connection between formation history and the masses of progenitor pancakes and filaments.

A very recent paper by Wang et al. (2006) suggests that the age dependence of clustering observed by GSW05 is really caused by mass stripping due to the large scale tidal field, which makes small old haloes appear less massive than their initial density field would suggest. This might provide an intuitive explanation for the effect, and is an example of an effect which could be connected to our scenario.

By studying conditional mass functions for the sheets and filaments in which the material of low-mass $z = 0$ haloes was embedded at early times, we found typical masses for progenitor pancakes at $z = 2$ which are significantly smaller than suggested by Mo et al. (2005). In addition, these progenitor masses depend strongly on the mass of the final halo. These results suggest that preheating due to the collapse of progenitor pancakes is insufficient to suppress later cooling and condensation of gas. It is nevertheless interesting that the sheet mass function is more strongly peaked than its halo counterpart, so that the majority of low-mass haloes were indeed embedded in more massive pancakes at $z \sim 2$.

In summary we argue that this work may provide an interesting and intuitive route to understanding how environment influences halo formation. It is important that analytic methods are refined to account at least qualitatively for the relatively strong effects seen in N-body simulations, and our results provide a first step in this direction. To build on the approach presented here it will necessary to model in more detail how the structural elements of the cosmic web influence the formation of haloes within them. We hope our results will motivate such efforts.

REFERENCES

- Bardeen J.M., Bond J.R., Kaiser N., Szalay A., 1986, ApJ, 304, 15
- Bond J.R., Cole S., Efstathiou G., Kaiser N., 1991, ApJ, 379, 440
- Bond J.R., Myers S., 1996, ApJS, 103, 1
- Bower, R.J., 1991, MNRAS, 248, 332
- Chandrasekar, S., Rev.Mod.Phys., 15, 2

- Chiueh T., Lee J., 2001, ApJ, 555, 83
 Croton D., Gao L., White S.D.M., astro-ph/0605636
 Doroshkevich, 1970, Astrofizika, 3, 175
 Gao L., Springel V., White S.D.M., 2005, MNRAS, 363, L66
 Lacey C., Cole S., 1993 MNRAS, 262, 627
 J. Lee, 2006, astro-ph/0605697
 Lin L., Chiueh T., Lee J., 2002, ApJ, 574, 527
 Mo H.J., White S.D.M., 1996, MNRAS, 282, 347
 H.J. Mo, X. Yang, F. C. van den Bosch & N. Katz, MNRAS 363, 11555 (2005)
 H.Y. Wang, H.J. Mo, Y.P. Ying (2006) astro-ph/0608690
 Percival W.J., 2001 MNRAS, 327, 1313
 Press W., Schechter P., 1974, ApJ, 187, 425
 Shen, J., Abel, T., Mo, H.J., Sheth, R.K., 2006, ApJ, 645, 783
 Sheth R.K., Mo H.J., Tormen G., 2001, MNRAS, 323, 1
 Sheth R.K., Tormen G., 2002, MNRAS, 329, 61
 Sheth R.K., Tormen G., 2004, MNRAS, 350, 1385
 Springel V. et al., 2005, Nat, 435, 639
 Wechsler, R.H. et al., 2005, astro-ph/0512416
 White S.D.M., 1996, in Schaeffer R. et al., eds, Cosmology and Large-scale Structure, Proc. 60th Les Houches School, ASP Conf. Ser., Vol. 176. Elsevier, Amsterdam, p. 349

APPENDIX A: THE ELLIPSOIDAL COLLAPSE MODEL

For convenience we here review the most important features of the ellipsoidal collapse model of BM96.

Starting from a homogeneous ellipsoidal patch with density contrast δ , the general equation that governs the collapse of an initially spherical surface along principal axis k is

$$\frac{d^2 A_k}{dt^2} = -4\pi G \bar{\rho} A_k \left[\frac{1+\delta}{3} + \frac{b'_k}{2} \delta + \lambda'_k \right] \quad (\text{A1})$$

where $b'_k \delta/2$ and λ'_k denote the interior and exterior tidal forces respectively. The interior tidal forces can be calculated for a constant density patch from the potential theory of homogeneous ellipsoids (cf. Binney & Tremaine 1987), and are given by:

$$b'_k = -\frac{2}{3} + \prod_{i=1}^3 a_i \int_0^\infty \frac{d\tau}{(a_k^2 + \tau) \prod_{j=1}^3 \sqrt{a_j^2 + \tau}}. \quad (\text{A2})$$

The linear approximation for external tides is:

$$\lambda'_{extk} = \frac{a}{a_i} \left[\lambda_k(t_i) - \frac{\delta_i}{3} \right] \quad (\text{A3})$$

where the λ_k s are the initial eigenvalues of the deformation tensor. The evolving quantity A_k relates to the boundary radius of the Lagrangian sphere, R through $A_k(t) = a_k(t)R$, so that the a_k can be thought of as the anisotropic generalisation of the standard cosmic expansion factor. We should note here that these equations are valid only in cosmological models with vanishing cosmological constant – a discussion of the modifications for a non-zero cosmological constant can be found in BM96.

The initial conditions are set by the Zel'dovich approximation

$$A_k(t_i) = a_i [1 - \lambda_k(t_i)] \quad (\text{A4})$$

$$\dot{A}_k(t_i) = H(t_i) A_k(t_i) - a_i H(t_i) \lambda_k(t_i) \quad (\text{A5})$$

The differential equations A1 are evolved for all axes k until a value of $A_k = 0.177a$ has been reached, after which the individual A_k are held constant. The factor of 0.177 results from the requirement that the virial density contrast of 179 obtained from spherical top hat calculations is reproduced.

APPENDIX B: INVARIANTS AND VARIABLES

The three rotational invariants of the 3×3 deformation tensor are

$$I_1 = \lambda_1 + \lambda_2 + \lambda_3 \quad (\text{B1})$$

$$I_2 = \lambda_1 \lambda_2 + \lambda_2 \lambda_3 + \lambda_3 \lambda_1 \quad (\text{B2})$$

$$I_3 = \lambda_1 \lambda_2 \lambda_3. \quad (\text{B3})$$

They can all be easily expressed in terms of the y_i s. It would therefore be useful if we could express our barrier variables in terms of these invariants.

The first barrier variable is naturally the density contrast, $\delta = I_1 = y_1$. The second variable chosen by CL01, is a combination of the first two invariants

$$r^2 = 3/2 I_1^2 - 2 I_2 = \frac{1}{3} \sum_{i \neq j} (\lambda_i - \lambda_j)^2 \quad (\text{B4})$$

which satisfies the condition that it is *independent* of y_1 . This is important both since we need to fit the density contrast at collapse to the barrier parameter, and because it means that it vanishes in the spherical case. (The spherical case is equivalent to $y_{i \neq 1} = 0$.)

For the third barrier variable a similarly convenient combination of the three invariants would be

$$u^3 = \frac{1}{9} (2 I_1^3 - 9 I_1 I_2 + 27 I_3) \quad (\text{B5})$$

which is also independent of y_1 and thus also vanishes in the spherical case.

The two variables r^2 and u^3 may be obtained directly from the y s as follows:

$$r^2 = \frac{2}{15} (y_2^2 + y_3^2 + y_4^2 + y_5^2 + y_6^2) \quad (\text{B6})$$

$$u^3 = \frac{1}{9} \frac{1}{25} (-3\sqrt{5}\sqrt{3}y_5^2 y_2 - 3\sqrt{5}y_5^2 y_3 + 6\sqrt{5}y_6^2 y_3 + 3\sqrt{5}\sqrt{3}y_4^2 y_2 - 3\sqrt{5}y_4^2 y_3 + 6\sqrt{5}y_2^2 y_3 + 2 - \sqrt{5}y_3^3 - 6\sqrt{5}\sqrt{3}y_4 y_5 y_6) \quad (\text{B7})$$

where we have used the explicit formulae in Lin et al. (2002)(LCL02). We thus have two variables which are expressed in terms of the rotational invariants and which are independent of the density contrast. The question is whether a barrier in these two variables is capable of capturing the behaviour of the ellipsoidal collapse model, and here we stumble upon a problem:

Although the transformation involved is one-to-one it does not guarantee that it will allow one variable to be a single valued function of the two others. Indeed it is easy

to show that transforming from eigenvalue space to δ, r^2, u^3 occasionally yields identical r and u values for different δ_c s - thereby preventing an expression of δ_c as a single valued function of the other two variables.

It proves significantly more accurate to express the barrier variables as suitable orthogonal linear combinations of the eigenvalues as follows

$$\delta = \lambda_1 + \lambda_2 + \lambda_3 \quad (\text{B8})$$

$$v = -\lambda_1 + \lambda_2 \quad (\text{B9})$$

$$w = -\lambda_1 - \lambda_2 + 2\lambda_3. \quad (\text{B10})$$

The variables v and w both vanish in the spherical case, are independent of δ and of each other, and are always positive for ordered eigenvalues $\lambda_1 < \lambda_2 < \lambda_3$. Since we prefer to work with a barrier which reproduces the ellipsoidal collapse model of BM96 as well as possible, we use this set of variables throughout our work.

The joint probability distribution can be found by manipulation of eqn. (14)

$$p(\delta, v, w|\sigma) = \frac{1}{3} \frac{15^3}{2^6} \frac{1}{\sqrt{5}\pi\sigma^6} \exp\left(-\frac{1}{2\sigma^2}(\delta^2 + \frac{15}{4}v^2 + \frac{5}{4}w^2)\right) \times (w^2 - v^2)v, \quad (\text{B11})$$

where the limits are

$$-\infty < \delta < \infty \quad (\text{B12})$$

$$0 \leq v \leq w \quad (\text{B13})$$

$$0 \leq w < \infty \quad (\text{B14})$$

The expectation values of v and w for a given σ are

$$\langle v \rangle = \frac{3\sigma}{\sqrt{10\pi}} \quad (\text{B15})$$

$$\langle w \rangle = \frac{9\sigma}{\sqrt{10\pi}}. \quad (\text{B16})$$

These are the values used to obtain the average barrier functions in figure 1 in the main text.

This paper has been typeset from a T_EX/ L^AT_EX file prepared by the author.